Carbon Nitride Thin Film-Sensitized Graphene Field-Effect Transistor: A Visible-Blind Ultraviolet Photodetector

Tamilarasan Palanisamy, Somak Mitra, Nitinkumar Batra, Jasmin Smajic, Abdul-hamid Emwas, Iman Roqan, Pedro Costa

Carbon Nitride Thin Film Sensitized Graphene Field-Effect Transistor: A Visible-blind Ultraviolet Photodetector

Tamilarasan Palanisamy[1,2,*], Somak Mitra[1], Nitinkumar Batra[1,4], Jasmin Smajic[1], Abdul-Hamid Emwas[3], Iman Roqan[1], Pedro M. F. J. Costa[1]

[1] King Abdullah University of Science and Technology (KAUST), Physical Science and Engineering Division, Thuwal 23955-6900, Saudi Arabia

[2] Electronics and Electrocatalysis Division (EEC), CSIR-Central Electrochemical Research Institute (CECRI), Karaikudi 630003. Tamilnadu. India.

[3] King Abdullah University of Science and Technology (KAUST), Imaging and Characterization Core Lab, Thuwal 23955-6900, Saudi Arabia

[4] Jean Rouxel Institut Des Materiaux, CNRS-University of Nantes, Nantes, 44300, France.

*Corresponding author: tamilan.krr@gmail.com

Abstract

Ultraviolet photodetectors often suffer from the lack of spectral selectivity due to strong interference from visible light. Exceptional electrical properties of graphene and unique optical properties of carbon nitride thin film (CNTF) have been integrated in this study for visible-blind ultraviolet photodetectors. Polycrystalline CNTFs were deposited by thermal vapour condensation method with good control over thickness in the 12 – 94 nm range. These thin films had considerable amount of sp^2 nitrogen deficiency compared to bulk carbon nitride powder that changes with thickness of the film. A unique optical absorption profile (in the ultraviolet-visible range) is obtained for CNTFs with wider band gap than their bulk counterpart. The absorbance falls sharply above 400 nm making CNTFs suitable for ultraviolet photodetection. A graphene field effect transistor (GFET) sensitized with CNTFs shows 10^3 A/W responsivity to ultraviolet radiation which falls rapidly to a negligible value in the visible spectrum. Developed photodetector shows a quick response and recovery time of 0.5 and 2.0 s, respectively. The effect

of film thickness on the photoresponse has also been determined. The findings would pave the simple route for development of sensitive, visible-blind ultraviolet photodetectors.

Keywords: Carbon nitride; Thin film; GFET; Ultraviolet; Visible-blind; Photodetector.

1. Introduction

Ultraviolet (UV) radiation is highly useful in fluorescence imaging, phototherapy and germicide devices. In small doses, it is essential for the production of vitamin D in our bodies. Conversely, the prolonged exposure to UV rays is generally harmful to living organisms, causing cataracts, skin cancer, severe sunburn, accelerated aging and, ultimately, damage to DNA (1). Detecting and measuring the intensity of UV radiation is, therefore, a critical healthcare issue.

In UV photodetectors, there is often strong response interference from the unintentional absorption of visible light by the photoactive element. For the most part, this is circumvented by rejection filters (2). Still, the development of sensing elements that are specific to the desired portion of the electromagnetic spectrum is preferable as it would simplify the device structure and reduce manufacturing costs. Hence, in the past decades, there has been a considerable effort to develop UV sensors that are blind to visible radiation (i.e. in the wavelength range of 300-700 nm) (3).

Graphitic carbon nitride (g-C_3N_4) is a non-metallic semiconductor with polymeric-chain triazine units (these can be also heptazine units, a.k.a. tris-s-triazine), arranged into a 2-dimentional structure (4). Due to its exceptional electronic and optical properties, this material has found use in diverse application fields, from biomedical devices to photocatalysis (5, 6). In the optoelectronics arena, the g-C_3N_4 has been widely exploited as the active element in photodetectors (7-9), light emitting diodes (10-12) and solar cells (13-15). As concerns photodetectors, the strong electron-hole pair generation upon optical absorption makes g-C_3N_4 a suitable sensing element for these devices (7). For instance, an organic-inorganic hybrid composite of g-C_3N_4 based photodetector has been demonstrated with broad absorption to cover

ultraviolet and visible range (8). Prakash et al. reported a similar ultra-broadband photodetector using g-C_3N_4-Si heterojunction (9). In these examples, bulk and exfoliated nanosheets of g-C_3N_4 were used and both showed broadband absorption (covering the whole visible and a part of UV spectrum), thereby resulting in poor spectral selectivity for UV detectors.

A latest technological advancements g-C_3N_4 synthesis is carbon nitride thin films (CNTFs) with good control over surface uniformity which also have shown unique optoelectronic properties (16). Interestingly, CNTFs have shown narrow optical absorption band in UV region (16, 17). Although easy methods, such as drop casting and spin coating of exfoliated ultra-thin flakes of g-C_3N_4, have been developed, they fail to produce uniform, transferrable, large-area thin films (18, 19).

Among the physical vapour deposition methods, thermal vapour condensation attained wider appreciation due to its simple instrumentation and competitive film quality (20). Bian et al., have deposited uniform CNTF where they demonstrated the easily tuneable morphology and thickness through the choice of substrate and quantity of precursor, respectively (18). A centimetre-size polymeric CNTF was deposited by thermal vapour condensation and polymerization of melamine on nitrogen-doped graphene substrate (19). A similar method could result in the deposition of high quality boron doped CNTFs by simultaneous vapour phase deposition and polymerization of melamine and boric acid (21).

Following the above, it has been possible to fabricate devices based on CNTFs. A Schottky photodiode using CNTF and p-type silicon has been developed for white light detection, where the CNTF was deposited by the pyrolysis of a film containing hexamethylenetetramine and urea (22). Recently, the growth of wafer-scale two-dimensional CNTF by a vapour-phase transport-

assisted condensation method and subsequent use for the fabrication of photodetector array is reported (23).

Despite its advantageous physicochemical properties, non-toxicity, low cost and high stability, the applications of carbon nitrides in photo energy conversion applications are greatly limited due to the rapid recombination of photogenerated electron-hole pair and short carrier diffusion (24). Interestingly, several authors claim that the heterojunction of g-C_3N_4 with graphene separates photogenerated charge carriers, effectively, in optoelectronic devices (25-28). On the other hand, graphene is well known for its ultra-narrow band gap which promoted graphene field effect transistors (GFET) as an ultra-wide band photodetector (29-33). Nevertheless, the poor spectral selectivity (given its wider spectral response) and low photo current generation (due to poor light absorption, ~ 2.3 % per sheet under visible light), are the long-term bottlenecks (34).

In this work, we combined a thin film of g-C_3N_4 and a GFET to fabricate a highly sensitive, and selective, photodetector for UV light detection. In doing so, we also developed a simple methodology to deposit and transfer wafer-scale, thickness-controlled CNTF. Critically, our CNTF-sensitized GFET photodetector (CNTF-GFET) operates under ultraviolet light, with negligible interference from the visible spectral region.

2. Experimental section

2.1 Materials

Melamine and ferric chloride based copper etchant were purchased from Sigma-Aldrich. The quartz crucibles (height 50 mm, mouth diameter 50 mm, with lid) were purchased from Glasscolabs. Single layer graphene (SLG), with sheet resistance of 450 ± 40 Ohms/sq and grown

by chemical vapour deposition (CVD), was purchased from Graphenea, Spain. Heavily-doped p-type silicon wafer ($\rho = 0.001 – 0.005$ Ω-cm), with 300 nm thermally grown oxide, was purchased from University Wafers. Deionised water (resistivity of 18.2 MΩ cm) was used in water bath. All the reagents were used as-received, without further purification.

2.2 Carbon nitride thin film deposition

CNTFs were deposited by a simple one-pot thermal vapour condensation (TVC) method, as reported elsewhere (18). Melamine was used as a precursor for both the CNTF deposition and bulk g-C_3N_4 powder synthesis. A detailed schematic illustration of the CNTF deposition and transfer is given in †ESI Fig. S1. Briefly, 5 g of melamine was loaded into a quartz crucible and covered with a quartz substrate. The sample was heated at 3 °C/min using a muffle furnace. Melamine sublimed at around 345 °C (35) and the vapour condensed into a thin film on the substrate. As the deposition parameters and the crucible volume were the same, the film thickness depended only on the quantity of the melamine in the crucible. The deposited film was pyrolysed at 600 °C for 1 h in a self-produced environment to form CNTF with respective thickness (†ESI Fig. S2(a)). The thickness of CNTFs was measured using atomic force microscopy (AFM) after transferring the films on to an atomically flat Si substrate (†ESI Fig. S2(c & d)). CNTFs with different thickness are denoted as "CNTF-X" (X = 12, 25, 42, 54 and 90) where "X" is the thickness of the film in nanometres. The deposited thin films were hydrophobic and showed poor adhesion to the quartz surface. Hence, the film could be simply transferred to water by immersion and, subsequently, placed in other surfaces (†ESI Fig. S3). All samples (powder and films) were stored under vacuum and protected from light exposure.

2.3 Photodetector fabrication

The typical photodetector fabrication included two steps. In the first, the GFET was fabricated by transferring SLG onto an interdigitated electrode (IDE) of 20 μm channel length. Briefly, an IDE pattern with 20 μm channel length, 30 μm finger-width and 2 mm finger length was fabricated on a Si/SiO_2 substrate by a standard photolithography process using a positive photoresist (36). A gold film of 100 nm thickness along with a 5 nm titanium adhesion layer, were deposited by e-beam evaporation followed by the photoresist lift-off. Parallel to this, the copper foil from the commercial SLG was dissolved using a ferric chloride based etchant. The resulting PMMA-SLG film was washed thrice in a deionised water bath and finally exposed to a 10 % HCl solution. Afterwards, it was transferred to the gold IDE and baked at 100 °C, under vacuum and for 1 h, to enhance the SLG-to-Au adhesion. Finally, the PMMA supporting layer was dissolved in boiling acetone. In the second step, the CNTF was transferred onto the GFET using a water-assisted method (mentioned in section 2.2), followed by annealing (at 150 °C for 1 h) to ensure appropriate adhesion between the SLG and the CNTF. The FESEM image of the final CNTF-GFET device is given in †ESI Fig. S4. For control experiments, photodetectors with g-C_3N_4 powder (no SLG) were also fabricated by drop-casting the nitride's aqueous dispersion onto the IDE. Another control device was fabricated by transferring the CNTF-42 on IDE (no SLG). More details on thin film deposition, characterisation instruments and methods as well as device fabrication can be found in ESI.

3. Results and discussion

3.1 Structural analysis

The X-ray diffraction (XRD) patterns of g-C_3N_4 and CNTFs are given in Fig. 1. The powder XRD pattern of g-C_3N_4 shows the characteristic interplanar stacking peak of graphitic materials

at 27.5º corresponding to the (002) plane, with 0.32 nm interplanar separation. The g-C_3N_4 structure is denser than crystalline graphite (d_{002} = 0.335 nm) due to the stronger localization of electrons (37). The peaks at 12.8°, 17.7° and 21.8° indicate that the bulk g-C_3N_4 powder is composed of parallel chains of heptazine and triazine units (38). These peaks are notably absent in the grazing incident X-Ray diffraction (GIXRD) patterns of CNTFs. Similar observations were reported for exfoliated nanosheets (39). As per the transmission electron microscope (TEM) images (†ESI Fig. S2(b)), the CNTFs are porous with nanoscale topological features. Similar features were observed for nanoscheets (33) and possibly explain the absence of the peaks. Also of note, the (002) peak of the CNTFs is clearly shifted to higher 2θ values in direct proportion to the film thickness, further confirming the presence of a tightly packed structure (38). Further to this, the FWHM is increasing with thickness of the film (inset of Fig. 1) indicating a monotonically reduced crystallite size. Overall, the data suggests that increasing the thickness results in smaller and tightly packed g-C_3N_4 crystallites within the CNTFs.

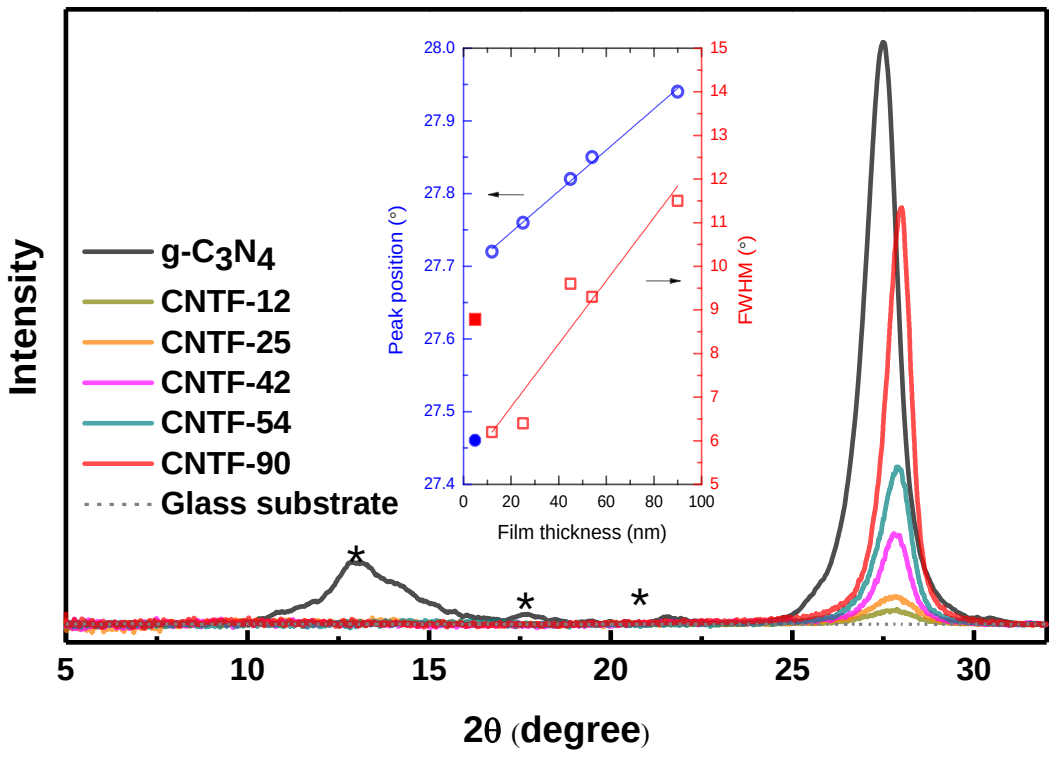

Fig. 1. GIXRD analysis of CNTFs. The intensity of CNTFs is 3 times magnified. Inset: Position and full width half maximum (FWHM) of (002) peak of CNTFs. The corresponding data of bulk g-C_3N_4 (filled symbols) are given for comparison.

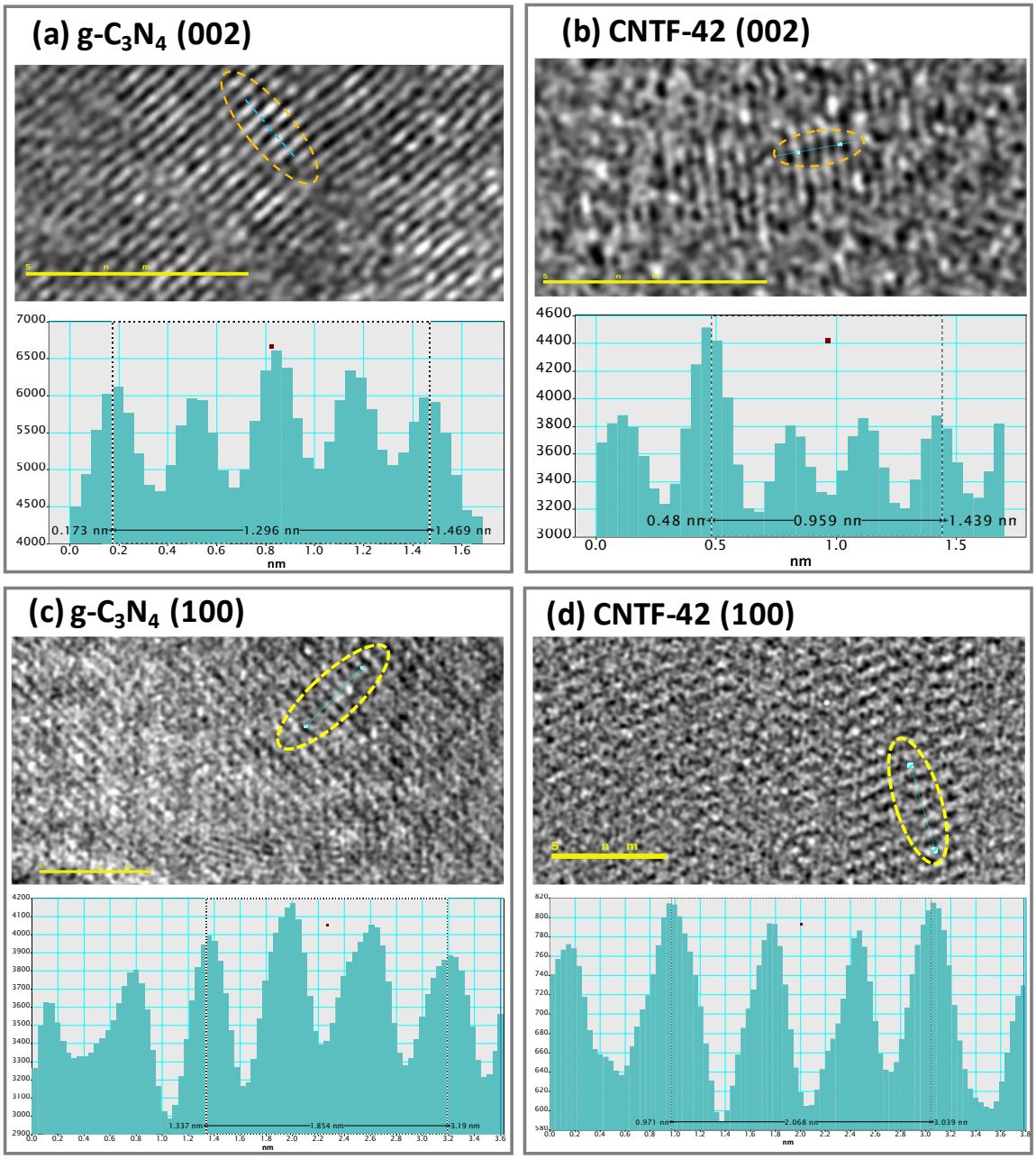

Fig. 2. HRTEM images of g-C_3N_4 and CNTF-42 along with the corresponding line profiles of the interplanar spacing of (002) and (100) planes.

3.2. Surface morphological and chemical analyses

The microstructure of the deposited CNTF has been analyzed using HRTEM and compared with the bulk g-C_3N_4 powder. Representative micrographs depicting (002) and (100) planes of the g-C_3N_4 and CNTF-42 are shown in Fig. 2, along with the line profile perpendicular to the lattice planes. In general, the g-C_3N_4 has clear (002) and (100) planes that correspond well with bigger crystallites than the CNTF-42. The line profiles reveal that the g-C_3N_4 and CNTF-42 have an average (002) interplanar distance of 0.324 and 0.319 nm, respectively. These are in good agreement with the observations from X-ray diffraction. On the other hand, the (100) planes are separated by 0.618 and 0.689 nm for the g-C_3N_4 and CNTF-42, respectively. The compressed (002) and expanded (100) interplanar distance could be due to a more ordered arrangement of the Melon chains within the crystallites. The SEM image of the CNTF-42 has also been recorded on an aluminium substrate (†ESI Fig. S5(a)). The energy dispersive X-ray spectrum (EDS) of the film (†ESI Fig. S5(b)) and corresponding elemental distribution map (†ESI Fig. S5(c & d)) clearly show the presence of C and N atoms.

3.3 Molecular vibrational spectroscopy

Typical transmission mode Fourier-transform infrared spectra (FTIR) spectra of the bulk g-C_3N_4 powder and CNTF-42 are shown in Fig. 3(a). The 1234 cm^{-1} mode is assigned to the sp^2 C=N bending vibrations, while the 1319 cm^{-1} signal comes from the out-of-plane bending vibrations of the heptazine units. For the g-C_3N_4, the strong signal at 806 cm^{-1} can be imputed to the breathing mode of heptazine units. This mode is quite weak in CNTFs due to the exfoliated sheet-like morphology(as observed by HRTEM) (40). The pendent amines (C-NH_2) at the sheet edges and the partially condensed bridging amines (C-(NH)=C) explain the signals of N-H

deformation (887 cm^{-1}), N-H bending (1403 cm^{-1}) as well as the primary (3270 cm^{-1}) and secondary amine (3200 cm^{-1}) modes (41). The broad mode around 3450 cm^{-1} is due to the O-H stretching from physically adsorbed moisture. In general, the modes between 1600 – 1700 cm^{-1} are assigned to C=C, C=N and C=O vibrations (42). Specifically, the band at 1631 cm^{-1} could be predominantly assigned to the C=N (or to the C=N-C) stretching vibrations. Nevertheless, there could be a significant contribution from C-C and N-N vibrations. The C-H stretching modes at 2850 (symmetric) and 2915 cm^{-1}(asymmetric) in both samples (suppressed by the N-H modes in g-C_3N_4) indicate the presence of a partially condensed phase (42).

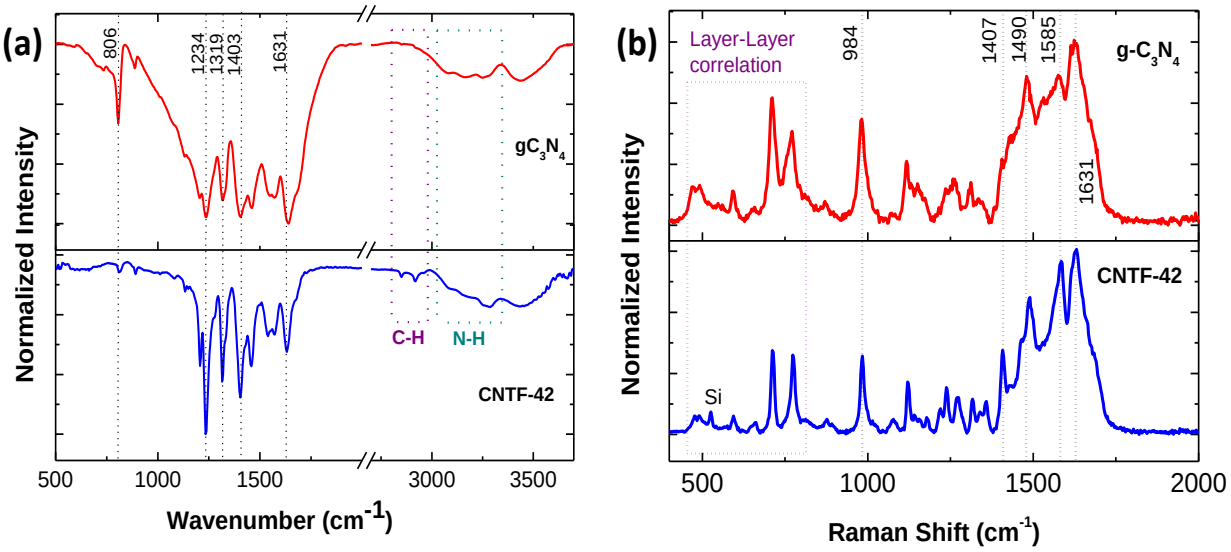

Fig. 3. Molecular vibrational spectra. (a) FTIR and (b) Raman spectra of bulk g-C_3N_4 and CNTF-42. The peak around 520 cm^{-1} in the Raman spectrum of CNTF-42 arises from the silicon wafer.

In general, the Raman spectra of g-C_3N_4 and CNTF-42 are identical (Fig. 3(b)), with some of the modes (1234, 1320, 1407 and 1631 cm^{-1}) also present in the corresponding FTIR spectra. Being graphitic structures, the Raman spectra of both materials have a broad background between 1380 and 1740 cm^{-1} (corresponding to G- and D-bands), convoluted with other 4 major peaks (1407,

1490, 1585 and 1631 cm^{-1}). Here, the modes at 1490 and 1585 cm^{-1} can be assigned to sp^2 C=N asymmetrical stretching and sp^3 N–C–N symmetrical stretching, respectively (43). Jiang et al. assigned the pairs of peaks at 491-591 and 711-773 cm^{-1} to correlation vibrations (due to the layer–layer deformation vibrations) (43). The peak at 984 cm^{-1} can be assigned to ring breathing modes of s-triazine units (44). We did not observe any significant signal between 2000 and 2500 cm^{-1} which indicates that both g-C_3N_4 and CNTF-42 have no N=C=N or C≡N groups (45).

3.4 Surface chemistry

The elemental composition of the deposited thin films was obtained by integrating the peaks in the X-ray photoelectron spectra (XPS) survey spectrum (†ESI Fig. S6) and compared with that of the g-C_3N_4 powder. The triplicate analysis concluded a stoichiometric formulae of $C_3N_{3.57\pm0.06}$ and $C_3N_{3.28\pm0.02}$ for the bulk powder and the thin film, respectively (†ESI Table S1). This clearly indicates a deviation from the stoichiometry of perfect g-C_3N_4. Moreover, the CNTF-42 is more N-deficient (or C-rich) compared to g-C_3N_4 powder. The stoichiometry of CNTF with various thicknesses was compared with g-C_3N_4 powder in order to understand the effect of thickness (†ESI Fig. S7). Interestingly, the nitrogen content gradually increases with thickness towards bulk carbon nitride. The current knowledge on the TVC-grown CNTFs is insufficient to explain the reason for this trend despite the growth conditions being the same.

The representative high-resolution C 1s spectra of g-C_3N_4 and CNTF-42 (Fig. 4(a)) have been deconvoluted into three major components, C – N = C (288.2 eV), C-NH_2 (286.2 eV) and C – C = C (284.7 eV). They contribute 90.2±1.1, 2.1±0.2 and 7.7±0.9 % for the g-C_3N_4 and 81.7±0.7, 2.1±0.7 and 16.2±1.2 % for the CNTF-42, respectively. The triplicate measurements (†ESI table S2) undoubtedly show a lower C – N = C contribution in the CNTF-42, while the C – C = C is

stronger. This indicates that a considerable amount of sp^2 nitrogen, from the *s*-triazine ring, has been replaced by carbon. Moreover, it is in good agreement with the determined stoichiometry.

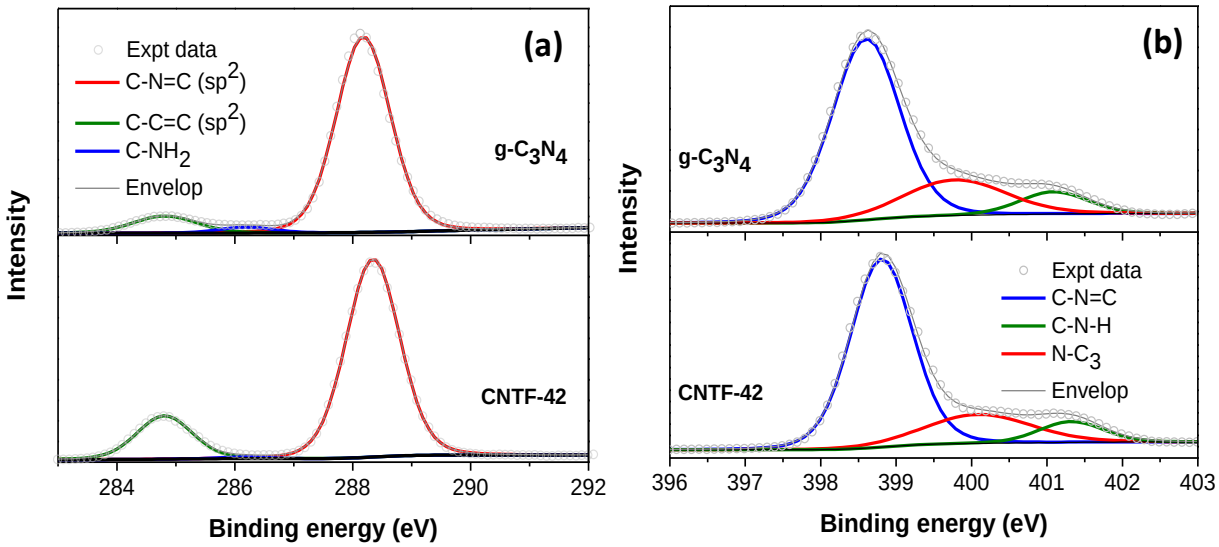

Fig. 4. High-resolution XPS of g-C_3N_4 and CNTF-42. (a) C 1s and (b) N 1s spectra with deconvoluted components showing the contributions. Refer to †ESI table S2 for the complete detail of the contribution of the individual components.

The pendent amine (C-NH_2) components from the partially condensed phases and edges of the carbon nitride sheets did not change much. Similarly to the C 1s peak, the high-resolution N 1s spectra (Fig. 4(b)) could be deconvoluted into three components, at 398.7 (C – N = C), 400 (N-C_3) and 401.2 eV (C – N – H). The corresponding fractions are 70.5±0.1, 20.8±0.2 and 8.8±0.1 % for the g-C_3N_4, and 72.2±0.5, 19.3±0.3 and 8.5±0.8 % for the CNTF-42, respectively. It is important to understand that the N 1s shows increased C – N = C fraction in the CNTF-42 (†ESI table S2), in contrast to C 1s spectra, because it is compared with N-C_3 and C – N – H, not with the C – C = C contribution. The N-C_3 signal arises from the bridging sp^3 nitrogen, while the C – N – H can be imputed to the partially-condensed bridging nitrogen or pendent amine. As the C 1s

spectra confirmed the stability of the pendent amine fraction, the 401.2 eV signal should be (mainly) composed by the partially condensed amine. The N-C_3 fraction is slightly decreased because of the formation of the C – C = C in CNTFs. Overall, the significantly lower N-C_3 and C – N – H composition in N 1s spectra point to an increased C – N = C fraction in CNTFs. However, this is misleading. In fact, it is decreased because of the C – C = C formation.

The gradual change in the C 1s and N 1s spectra with film thickness is given in †ESI Fig. S8. Interestingly, the C-N=C signal increases with film thickness following the same trend of the nitrogen elemental fraction, while the C – C = C follows an inverse relation. Considering the nearly unchanged pendent amine, we can conclude that the increase in elemental nitrogen is due to the increased sp^2 nitrogen in the ring. On the other hand, N-C_3 and C – N – H from the bridging are marginally decreasing.

3.5 Optoelectronic properties

The relation of the optical absorption spectra of g-C_3N_4 and CNTFs with various thicknesses is given in Fig. 5(a). The g-C_3N_4 powder leads to the conventional edge, at around 460 nm (46), while the CNTFs show it well within 400 nm (18, 47). The band gap of these semiconductors can be directly measured from the Tauc plot (Fig. 5(b)), by extrapolating the linear regression of the absorption edge. It is clear, from the representative Tauc plot, that CNTFs have a much wider band gap energy (generally, $E_g > 3$ eV) when compared to the g-C_3N_4 powder (2.4 eV). In general, a disordered g-C_3N_4 structure has a reduced band gap (46). On the other hand, the exfoliated g-C_3N_4 monolayers or the carbon nitride with s-triazine structure show a larger E_g (48, 49). In this context, the wider band gap of CNTFs could be imputed to the highly ordered (as per the XRD and HRTEM analysis) sheet-like microstructures (†ESI Fig. S2(b)). In single

compound materials, the considerable absorption at energies below the band gap arises from the formation of localized states (Urbech tail and Weak absorption tail) at the boundaries of band gap due to the structural disorder in the material (50). As the absorption tail (immediately after the absorption edge) is smaller than in g-C_3N_4, the CNTFs should have less defect-induced localized states.

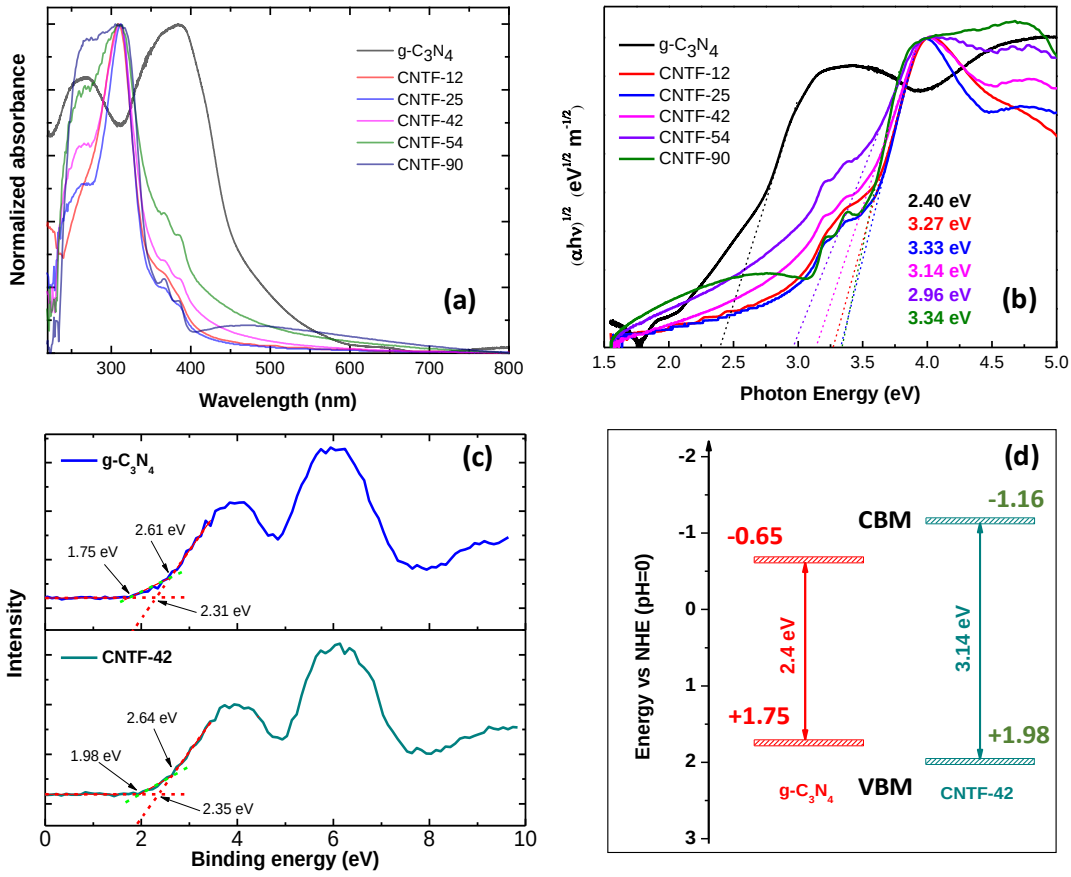

Fig. 5. Optical properties of g-C_3N_4 and CNTFs. (a) Optical absorption spectra in the ultraviolet-visible range, (b) Tauc plot, (c) XPS valence band spectra, and (d) schematic illustration of band position.

To determine the band edges of g-C_3N_4 and CNTF-42, their XPS valence band spectra (Fig. 5(c)) were analyzed. Two major features have been identified, including the N 2p states (around 6 eV).

Although the extrapolated valence band edges (2.31 and 2.35 eV) are nearly the same, their offsets differ (1.75 and 1.98 eV), respectively (46). It is reasonable to take these offset values as the valence band maximum (VBM). Considering the band gap and VBM of g-C_3N_4 and CNTF-42, the conduction band minimum (CBM) is calculated to be at -0.65 and -1.16 eV, respectively (Fig. 5(d)).

The photoluminescent (PL) spectrum of CNTF-90 (†ESI Fig. S9) shows a strong emission peak at 467 nm which is blue-shifted to 437 nm (CNTF-12) at the minimal thickness considered. Interestingly, another emission peak at 540 nm emerges with thinner films. The relative intensity of this peak is quite significant in CNTF-12 and CNTF-25. Zhang et al., have observed a gradual red-shift and peak broadening in PL emission of carbon nitride with TVC temperature (300 – 650 ºC) due to different degree of the condensation and disorder (51). Therefore, it is wise to attribute the emerging peak to the degree of condensation of CNTFs with different thicknesses. The PL spectra and corresponding discussion are available in †ESI 5. The time-resolved photoluminescence (TRPL) of the CNTFs was analyzed to understand the speed of charge recombination. The decay curves of CNTFs (†ESI Fig. S10) with 12, 25, 45 and 54 nm thickness were measured with the corresponding PL emission peak, using a 280 nm excitation. The fluorescence lifetime of the CNTFs has been extracted from the experimental data by double-exponential fitting. Table S3 (†ESI 5) clearly shows that both time constants are increasing with thickness. For an effective transfer of photoinduced charges, the CNTF should have higher time constant. Moreover, the electronic properties of g-C_3N_4 and CNTFs were analyzed by electron paramagnetic resonance (EPR) under dark and illuminated (365 nm) conditions (†ESI Fig. S11). The tested carbon nitride samples show a single Lorentzian feature around 2.002 g-factor value, generally from the unpaired electron localized at the sp^2 C atoms of the π-bonded aromatic

structure (52). Since it is difficult to estimate the amount of CNTF exposed to microwaves, we are not comparing the EPR signal strength of the samples. But the more important feature of this analysis is the nearly 30 % photoinduced enhancement of the EPR signal for CNTFs while it was only 4.5 % for the g-C_3N_4 powder. As discussed in section 3.4, the CNTFs have more two-coordinated nitrogen vacancies which could donate unpaired electrons to adjacent carbon atoms and enhance the overall photo-response of the sample (5). We did not observe any trend in photoinduced EPR intensity enhancement with film thickness.

3.6 Photodetector performance

The above physico-chemical characterization clearly indicated that the CNTFs have comprehensive advantages over their bulk counterpart. Inspired by a previous report (28) and the optoelectronic properties exhibited, we demonstrate the potential application of CNTFs as ultraviolet photodetectors free from the interference of visible light.

The transfer curves of the GFETs are given in †ESI Fig. 12. All the fabricated GFETs had Dirac point voltage (V_{Dirac}) above 10 V confirming the p-doped graphene. GFETs with V_{Dirac} between 10 – 20 V were only used for CNTF-GFET photodetector fabrication. The devices tested in ambient conditions showed a negative current at all V_{GS} and is not stable (†ESI Fig. S13). Lai et al. have observed a similar phenomenon with g-C_3N_4 nanosheet based GFET photodetector and have attributed to the absorption of oxygen-containing impurities (28). Therefore, the devices were tested under vacuum. A shift in V_{Dirac} to higher positive potentials by 4.2±0.8 V was observed (Fig. 6(a)) when CNTFs were transferred onto the SLG channel. Upon illumination with ultraviolet light (λ = 310 nm), the transfer curve of SLG shift to lower potentials. As reported by Lai et al., the photogenerated electrons in CNTFs are transferred to graphene

resulting in net n-type doping which shift the V_{Dirac} with respect to the Fermi level (28). Moreover, the shift in transfer curve is gradually increasing with light intensity due to the proportional increase in photogenerated electrons. It is important to note that the shift in hole-conduction region is more significant than electron-conduction region with illumination power. As discussed in †ESI 6, the hole-conducting region has significantly higher $I_{DS}(V = 0)/I_{DS}(V = V_{Dirac})$. Therefore, the characteristics of the photodetectors have been determined at V_{GS} = 5V. Photoresponse of the device at different power of illumination (λ = 310 nm) has been calculated by subtracting it by the dark current of current-voltage (*I*-*V*) characteristics (Fig. 6(b)). The photocurrent (I_{ph}) increases linearly with V_{DS} at a constant V_{GS} and illumination power (P) due to the shorter transit time ($\tau_t = L^2/\mu V_{DS}$, where L is the length of the channel and μ is the mobility of the electrons) of the charge carrier in the channel under higher bias voltage (53). The corresponding responsivity is calculated by dividing the photocurrent with the light intensity ($R_{ph} = I_{ph}/P$).

Fig. 6(d) gives the intensity dependent photocurrent and responsivity at V_{DS} = 0.5 V, V_{GS} = 5 V and λ = 310 nm. The I_{ph} tends to saturation at higher light intensities. The quantitative dependence of the photocurrent on the light intensity is given by $I_{ph} = AP^{\alpha}$, where A is a constant and α is an exponent. The mathematical fitting to the experimental data yields $I_{ph} \propto P^{0.44}$ giving 0.44 for the exponent. The responsivity is clearly higher at lower incident power in agreement with previous reports (28, 54). The dependence of the responsivity on the light intensity ($R_{ph} = AP^{\alpha-1}$) also gives $\alpha = 0.44$ from $R \propto P^{-0.56}$ (Fig. 6(d)). The value of exponent close to 0.5 indicates that the photocurrent saturation is predominantly due to the kinetics of the photogenerated charge carriers recombination (54). The accelerated charge carrier recombination

could be attributed to (i) generation of electric field by photogenerated carriers that opposes the build-in electric field (28) and (ii) the trap states in the material (55).

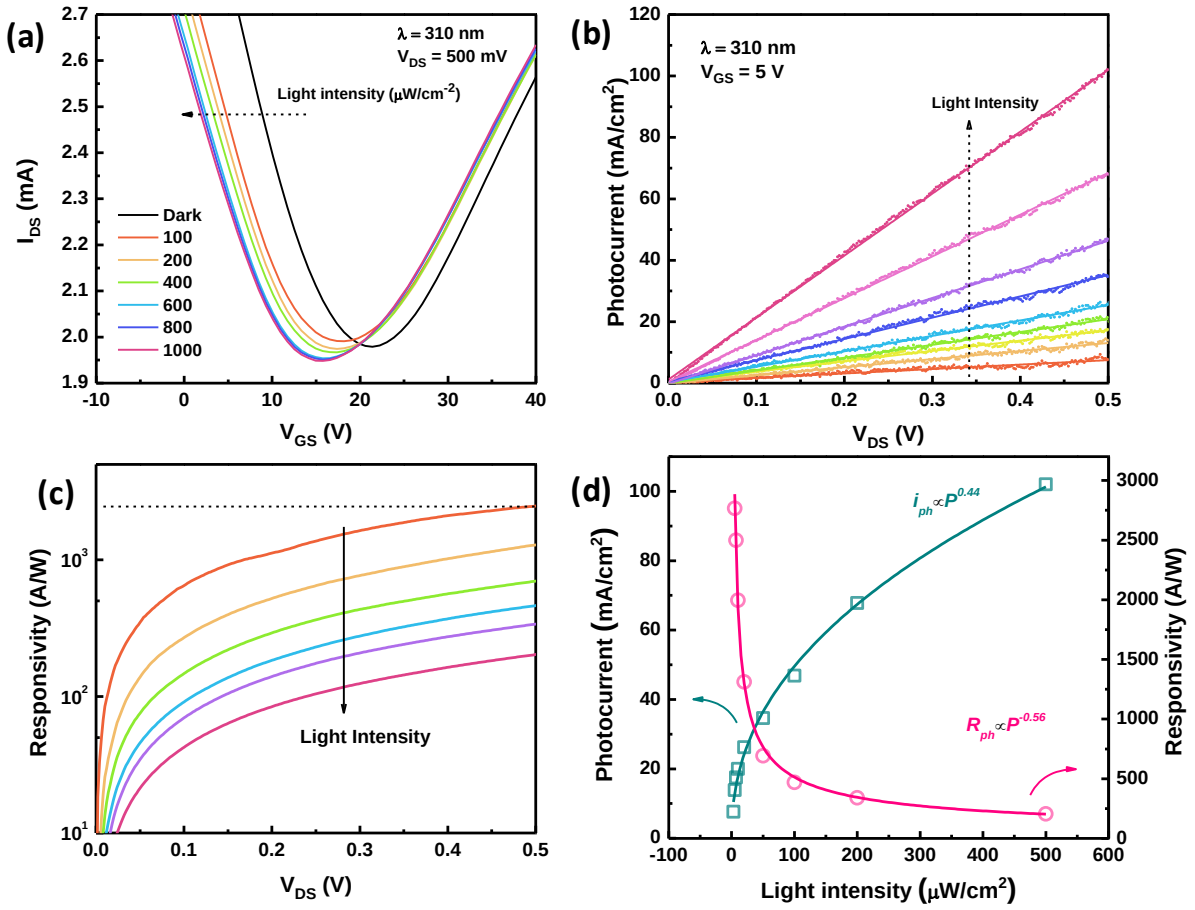

Fig. 6. Photoresponse of the CNTF-GFET with active area of 3.284x10^{-3} cm^2. (a) Transfer curve, (b) *I-V* characteristics, (c) responsivity at various light intensities at V_{GS} = 5 V and λ = 310 nm and (d) dependence of photocurrent and responsivity on the light intensity (V_{DS} = 0.5 V).

The typical temporal photoresponse to 100 μW/cm^2 ON/OFF illumination cycles of the CNTF-GFET photodetector with active area of 3.284x10^{-3} cm^2 is given in Fig. 7(a) at a V_{DS} bias of 0.5 V, where the V_{GS} was set to V_{Dirac}±10 V for all the devices. In these studies, V_{Dirac} of CNTF-

GFET at dark has been taken as reference. The operation at electron conduction region are standardized with $V_{GS} = V_{Dirac}+10$ V while it is set to be $V_{Dirac}-10$ V for hole conduction region. For reference, a GFET without CNTF sensitization has also been tested which shows very low negative photocurrent for $V_{GS} = V_{Dirac}+10$ V in agreement with literature (28). But the CNTF-GFET photodetector shows around 100 μA upon 310 nm light illumination. The ON/OFF illumination cycle clearly shows the fast response and recovery in the electron conduction region. The switching ratio of the device is given by $SR = (I_{ph}-I_d)/I_d$, where I_d is the dark current. The device shows a large switching ratio of 110 in the electron-conducting region.

On the other hand, the device delivered an improved I_{ph} and SR of around 135 μA and 157 at the hole-conduction region, respectively. This is in good agreement with the observation from transfer characteristics of the device. Moreover, the polarity of the signal also has been changed to the negative indicating the charge carrier switching. This phenomenon can be further understood by analyzing the photocurrent as a function of gate voltage (Fig. 7(b)). The SLG used in this study is naturally p-type doped. When V_{GS} is more negative from V_{Dirac}, a positive charge is induced in graphene resulting in a p-doping effect. Upon illumination, the increase in photogenerated electrons decreases the conductivity of the channel resulting in a decrease in current from the baseline. When V_{GS} approaches the V_{Dirac} of the illuminated device (V_0), the density of electrons and holes tends to be the same and thus the photocurrent approaches zero. At this potential the device is effectively switched off. On the other side, the photogenerated electrons boost I_{DS} in the electron conduction region. However, the device records lower responsivity in the electron-conduction side than the hole-conduction side as the SLG is inherently a p-type material. In order to highlight the combined advantage of CNTFs and GFET, we have tested a “CNTF only” device without SLG (†ESI Fig. S14(a)). The device did not show

any significant photocurrent despite the channel being biased with higher potential (up to 2 V). Similarly, a photodetector using g-C_3N_4 on GFET (g-C_3N_4-GFET) has been compared with CNTF-GFET, which shows *SR* = 2.5 only ((†ESI Fig. S14(b)). These values clearly indicate the superior performance of CNTF-GFET photodetectors.

A good sensor should have fast response and quicker recovery into the original state. Therefore the raising and decaying sides of the temporal response were analyzed using a double exponential function.

$$I_{ph}(t) = I_d + A_1 \exp(t/\tau'_{res}) + A_2 \exp(t/\tau''_{res}) \text{ ----------(1)}$$

$$I_{ph}(t) = I_d + A_3 \exp(-t/\tau'_{rec}) + A_4 \exp(-t/\tau''_{rec}) \text{ ----------(2)}$$

Here, τ_{res}', τ_{res}'', τ_{rec}' and τ_{rec}'' are the respective first and second exponential response and recovery time constants. A mathematical fitting to the experimental data reveals the τ_{res}' and τ_{rec}' of 0.5 and 2.0 s for the operation at $V_{GS} = V_{Dirac}$+10 V, respectively. These are reasonably good speed of operation in practical applications. On the other hand, the $V_{GS} = V_{Dirac}$-10 V operation has these values at 6.1 and 14.7 s, respectively. Although the $V_{GS} = V_{Dirac}$-10 V operation has nearly 50 % higher I_{ph}, the response and recovery are slow.

The thickness of the CNTF also plays a major role as generally observed in the catalyst film thickness in photoelectrochemical systems (26, 56). Although carbon nitrides are cost-effective and cover a major portion of visible light, their shorter electron diffusion length is a major bottleneck in using them extensively for photoelectrochemical applications. The present study reports the effect of film thickness on the magnitude of photocurrent (Fig. 7(d)). The responsivity

of the CNTF-GFET photodetectors has inverse relation with film thickness. Particularly, CNTF-12 and CNTF-25 have substantially high responsivity compared to thicker films.

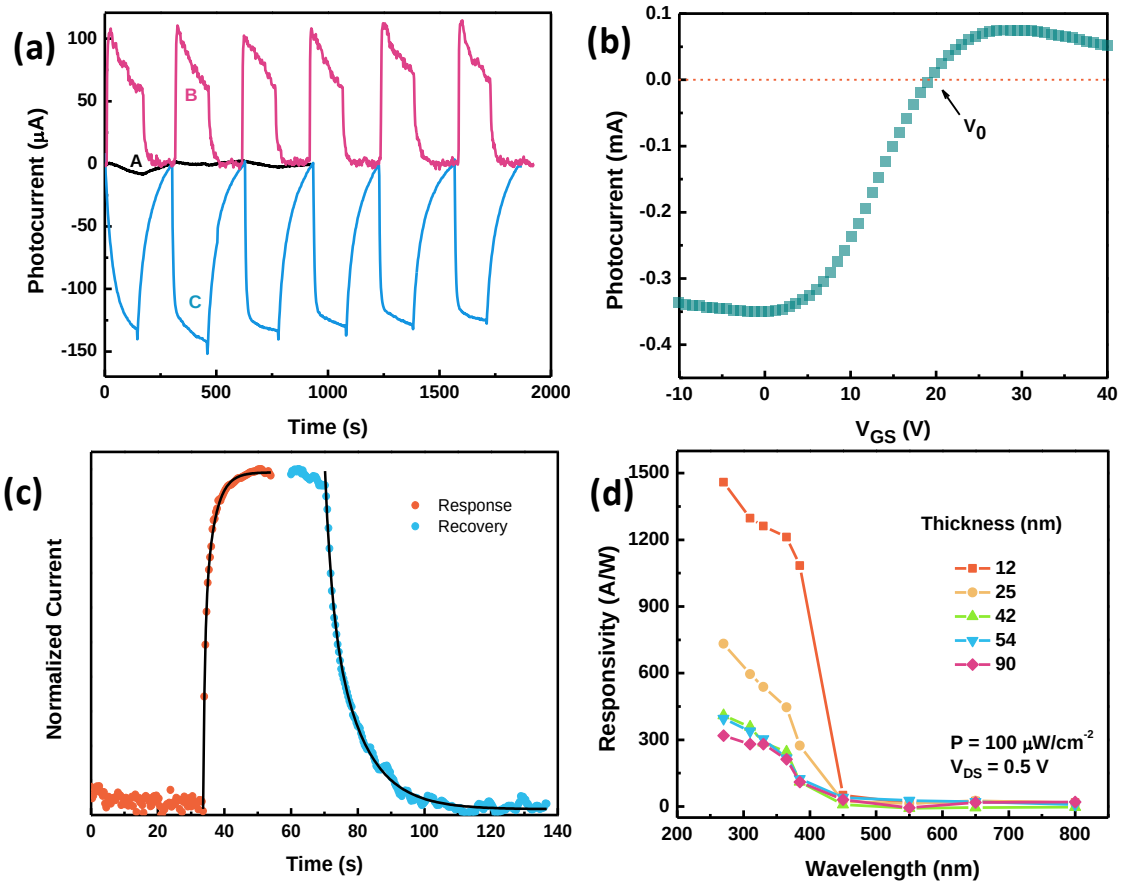

Fig. 7. Temporal photoresponse of the CNTF-GFET with active area of 3.284x10^{-3} cm^2, λ = 310 nm, P = 100 μW/cm^2, V_{DS} = 0.5 V and V_{GS}=V_{Dirac}+10V unless otherwise mentioned. (a) cyclic response and recovery pattern *((A) GFET with V_{GS}=V_{Dirac}+10V, (B) CNTF-GFET with V_{GS}=V_{Dirac}+10V and (C) CNTF-GFET with V_{GS}=V_{Dirac}-10V)*, (b) majority carrier switching behavior, (c) response and recovery of the signal and (d) CNTF thickness and wavelength dependence of the responsivity.

This is in contrast with the TRPL observations where the decay time constant increases with thickness. We expected higher decay time would result in better photogenerated electron-hole pair separation and thus better responsivity. However, the thicker films results in relatively lower photocurrent due to a shorter diffusion length that leads to higher carrier recombination. On the other hand, thinner films transfer photo-excited charge carriers into the graphene channel effectively despite having a lower amount of photoactive material per unit area. Therefore, the thickness of CNTFs predominantly affects the efficiency.

An interference-free ultraviolet photodetector should have negligible responsivity in the visible region. The wavelength dependent responsivity plot (Fig. 7(d)) shows that the responsivity of all the devices sharply falls around 400 nm following the trend in the optical absorption spectra (Fig. 5(a)). This is strong evidence that the CNTF-GFET photodetectors have negligible interference from visible light. The practical application of the CNTF-GFET photodetector is demonstrated using a 6 W multipurpose UV lamp (254 and 365 nm) and a 6 W lamp. It is clearly seen that the 254 nm radiation produces the strongest signal followed by the 365 nm, in agreement with experimental results. Moreover the white light produces a negligible signal and thus makes no significant interference.

4. Conclusion

In the present work, we have deposited carbon nitride thin film with tuneable thickness by thermal vapour condensation of melamine. The thin films were transferred onto desired substrates exploiting its hydrophobicity using a water-assisted method. These CNTFs are polycrystalline with tightly packed (002) planes compared to their bulk counterpart. Both the powder and thin film form of g-C_3N_4 showed nearly identical molecular vibrational spectra.

CNTFs have more nitrogen deficiency compared to g-C_3N_4 but the nitrogen content increases with film thickness. The optical absorption spectra of CNTFs indicate their selective absorption of UV radiation with band gap greater than 3 eV. Moreover, the conduction and valence band position changed. The light-induced EPR analysis shows at least 6-fold higher photogenerated charge carriers in CNTFs. These unique optoelectronic properties of CNTFs were exploited to develop CNTF-GFET photodetectors for UV radiation detection. These photodetectors showed up to 10^3 A/W responsivity, 157 switching rate, 0.5 s response and 2 s recovery time. Although the TRPL analysis indicated a higher decay time constant for thicker films, the photodetectors with thinner CNTFs showed better response due to the profound effect of shorter diffusion length. The device shows negligible response to visible light. Overall, the CNTF sensitized GFET photodetector is visible-blind, highly sensitive and selective to UV radiation.

5. Acknowledgement

We are grateful for the financial support from KAUST (BAS/1/1346-01-01). The Core Labs at KAUST are thanked for their technical assistance.

6. Reference

1. Schmalwieser AW, Weihs P, Schauberger G. UV Effects on Living Organisms. In: Meyers RA, editor. Encyclopedia of Sustainability Science and Technology. New York, NY: Springer New York; 2019. p. 1-63.
2. Lamkin I, Tarasov S, Petrov A, Menkovich E, Solomonov A, Kurin SY, editors. Research of the solar-blind and visible-blind photodetectors, based on the AlGaN solid solutions. Journal of Physics: Conference Series; 2014: IOP Publishing.
3. Chen H, Liu K, Hu L, Al-Ghamdi AA, Fang X. New concept ultraviolet photodetectors. Materials Today. 2015;18(9):493-502.
4. Wang A, Wang C, Fu L, Wong-Ng W, Lan Y. Recent Advances of Graphitic Carbon Nitride-Based Structures and Applications in Catalyst, Sensing, Imaging, and LEDs. Nano-Micro Letters. 2017;9(4):47.
5. Tu W, Xu Y, Wang J, Zhang B, Zhou T, Yin S, et al. Investigating the Role of Tunable Nitrogen Vacancies in Graphitic Carbon Nitride Nanosheets for Efficient Visible-Light-Driven H2 Evolution and CO2 Reduction. ACS Sustainable Chemistry & Engineering. 2017;5(8):7260-8.

6. Liao G, He F, Li Q, Zhong L, Zhao R, Che H, et al. Emerging graphitic carbon nitride-based materials for biomedical applications. Progress in Materials Science. 2020;112:100666.
7. Liu P, Sun Y, Wang S, Zhang H, Gong Y, Li F, et al. Two dimensional graphitic carbon nitride quantum dots modified perovskite solar cells and photodetectors with high performances. Journal of Power Sources. 2020;451:227825.
8. Velusamy DB, Haque M, Parida MR, Zhang F, Wu T, Mohammed OF, et al. 2D Organic–Inorganic Hybrid Thin Films for Flexible UV–Visible Photodetectors. Advanced Functional Materials. 2017;27(15).
9. Prakash N, Kumar G, Singh M, Barvat A, Pal P, Singh SP, et al. Binary Multifunctional Ultrabroadband Self-Powered g-C3N4/Si Heterojunction High-Performance Photodetector. Advanced Optical Materials. 2018;6(14):1800191.
10. Gan Z, Shan Y, Chen J, Qingfeng G, Zhang Q, Nie S, et al. The origins of the broadband photoluminescence from carbon nitrides and applications to white light emitting. Nano Research. 2016;9.
11. He L, Fei M, Chen J, Tian Y, Jiang Y, Huang Y, et al. Graphitic C3N4 quantum dots for next-generation QLED displays. Materials Today. 2019;22:76-84.
12. Tang W, Tian Y, Chen B, Xu Y, Li B, Jing X, et al. Supramolecular Copolymerization Strategy for Realizing the Broadband White Light Luminescence Based on N-Deficient Porous Graphitic Carbon Nitride (g-C3N4). ACS Applied Materials & Interfaces. 2020;12(5):6396-406.
13. Yan H, Tian X, Pang Y, Feng B, Duan K, Zhou Z, et al. Heterostructured g-C3N4/Ag/TiO2 nanocomposites for enhancing the photoelectric conversion efficiency of spiro-OMeTAD-based solid-state dye-sensitized solar cells. RSC Advances. 2016;6(104):102444-52.
14. Jiang L-L, Wang Z-K, Li M, Zhang C-C, Ye Q-Q, Hu K-H, et al. Passivated Perovskite Crystallization via g-C3N4 for High-Performance Solar Cells. Advanced Functional Materials. 2018;28(7):1705875.
15. Li Z, Wu S, Zhang J, Yuan Y, Wang Z, Zhu Z. Improving Photovoltaic Performance Using Perovskite/Surface-Modified Graphitic Carbon Nitride Heterojunction. Solar RRL. 2020;4(3):1900413.
16. Bian J, Huang C, Zhang R. Graphitic Carbon Nitride Film: An Emerging Star for Catalytic and Optoelectronic Applications. ChemSusChem. 2016;9 19:2723-35.
17. Jia F, Zhang Y, Hu W, Lv M, Jia C, Liu J. In-situ Construction of Superhydrophilic g-C3N4 Film by Vapor-Assisted Confined Deposition for Photocatalysis. Frontiers in Materials. 2019;6(52).
18. Bian J, Li Q, Huang C, Li J, Guo Y, Zaw M, et al. Thermal vapor condensation of uniform graphitic carbon nitride films with remarkable photocurrent density for photoelectrochemical applications. Nano Energy. 2015;15:353-61.
19. Gan X, Lv R, Zhang T, Zhang F, Terrones M, Kang F. Transferrable polymeric carbon nitride/nitrogen-doped graphene films for solid state optoelectronics. Carbon. 2018;138:69-75.
20. Muhl S, Méndez JM. A review of the preparation of carbon nitride films. Diamond and Related Materials. 1999;8(10):1809-30.
21. Giusto P, Arazoe H, Cruz D, Lova P, Heil T, Aida T, et al. Boron Carbon Nitride Thin Films: From Disordered to Ordered Conjugated Ternary Materials. Journal of the American Chemical Society. 2020;142(49):20883-91.
22. Gupta R, Al-Ghamdi AA, El-Tantawy F, Farooq W, Yakuphanoglu F. Novel photosensor based on carbon nitride thin films. Materials Letters. 2014;134:149-51.
23. Liu Z, Wang C, Zhu Z, Lou Q, Shen C, Chen Y, et al. Wafer-scale growth of two-dimensional graphitic carbon nitride films. Matter. 2021;4(5):1625-38.
24. Li K, Zhang W-D. Creating Graphitic Carbon Nitride Based Donor-π–Acceptor-π–Donor Structured Catalysts for Highly Photocatalytic Hydrogen Evolution. Small. 2018;14(12):1703599.
25. Fang H, Ma H, Zheng C, Lennon S, Wu W, Wu L, et al. A high-performance transparent photodetector via building hierarchical g-C3N4 nanosheets/CNTs van der Waals heterojunctions by a facile and scalable approach. Applied Surface Science. 2020;529:147122.

26. Peng G, Volokh M, Tzadikov J, Sun J, Shalom M. Carbon nitride/reduced graphene oxide film with enhanced electron diffusion length: an efficient photo-electrochemical cell for hydrogen generation. Advanced Energy Materials. 2018;8(23):1800566.
27. Du A, Sanvito S, Li Z, Wang D, Jiao Y, Liao T, et al. Hybrid graphene and graphitic carbon nitride nanocomposite: gap opening, electron–hole puddle, interfacial charge transfer, and enhanced visible light response. Journal of the American Chemical Society. 2012;134(9):4393-7.
28. Lai SK, Xie C, Teng KS, Li Y, Tan F, Yan F, et al. Polymeric Carbon Nitride Nanosheets/Graphene Hybrid Phototransistors with High Responsivity. Advanced Optical Materials. 2016;4(4):555-61.
29. Deng T, Zhang Z, Liu Y, Wang Y, Su F, Li S, et al. Three-Dimensional Graphene Field-Effect Transistors as High-Performance Photodetectors. Nano Letters. 2019;19(3):1494-503.
30. Ishida S, Anno Y, Takeuchi M, Matsuoka M, Takei K, Arie T, et al. Highly photosensitive graphene field-effect transistor with optical memory function. Scientific Reports. 2015;5(1):15491.
31. Deokar G, Genovese A, Surya SG, Long C, Salama KN, Costa PMFJ. Semi-transparent graphite films growth on Ni and their double-sided polymer-free transfer. Scientific Reports. 2020;10(1):14703.
32. Deokar G, Casanova-Cháfer J, Rajput NS, Aubry C, Llobet E, Jouiad M, et al. Wafer-scale few-layer graphene growth on Cu/Ni films for gas sensing applications. Sensors and Actuators B: Chemical. 2020;305:127458.
33. Deokar G, Genovese A, Costa PMFJ. Fast, wafer-scale growth of a nanometer-thick graphite film on Ni foil and its structural analysis. Nanotechnology. 2020;31(48):485605.
34. Falkovsky LA. Optical properties of graphene. Journal of Physics: Conference Series. 2008;129:012004.
35. Devallencourt C, Saiter JM, Fafet A, Ubrich E. Thermogravimetry/Fourier transform infrared coupling investigations to study the thermal stability of melamine formaldehyde resin. Thermochimica Acta. 1995;259(1):143-51.
36. Mack C. Fundamental Principles of Optical Lithography: The Science of Microfabrication: Wiley; 2011.
37. Thomas A, Fischer A, Goettmann F, Antonietti M, Müller J-O, Schlögl R, et al. Graphitic carbon nitride materials: variation of structure and morphology and their use as metal-free catalysts. Journal of Materials Chemistry. 2008;18(41):4893-908.
38. Fina F, Callear SK, Carins GM, Irvine JTS. Structural Investigation of Graphitic Carbon Nitride via XRD and Neutron Diffraction. Chemistry of Materials. 2015;27(7):2612-8.
39. YunYang, Lei W, Xu Y, Zhou T, Xia M, Hao Q. Determination of trace uric acid in serum using porous graphitic carbon nitride (g-C3N4) as a fluorescent probe. Microchimica Acta. 2017;185.
40. Kang Y, Yang Y, Yin LC, Kang X, Liu G, Cheng HM. An Amorphous Carbon Nitride Photocatalyst with Greatly Extended Visible-Light-Responsive Range for Photocatalytic Hydrogen Generation. Advanced Materials. 2015;27(31):4572-7.
41. Zhu B, Xia P, Ho W, Yu J. Isoelectric point and adsorption activity of porous g-C3N4. Applied Surface Science. 2015;344:188-95.
42. Colthup NB. Spectra-Structure Correlations in the Infra-Red Region. J Opt Soc Am. 1950;40(6):397-400.
43. Jiang J, Ou-yang L, Zhu L, Zheng A, Zou J, Yi X, et al. Dependence of electronic structure of g-C3N4 on the layer number of its nanosheets: A study by Raman spectroscopy coupled with first-principles calculations. Carbon. 2014;80:213-21.
44. Zinin P, Ming L-C, Sharma S, Khabashesku V, Liu X-R, Hong S, et al. Ultraviolet and near-infrared Raman spectroscopy of graphitic C 3N 4 phase. Chemical Physics Letters - CHEM PHYS LETT. 2009;472:69-73.

45. McMillan PF, Lees V, Quirico E, Montagnac G, Sella A, Reynard B, et al. Graphitic carbon nitride C6N9H3·HCl: Characterisation by UV and near-IR FT Raman spectroscopy. Journal of Solid State Chemistry. 2009;182(10):2670-7.
46. Kang Y, Yang Y, Yin L, Kang XD, Liu G, Cheng H-M. An Amorphous Carbon Nitride Photocatalyst with Greatly Extended Visible-Light-Responsive Range for Photocatalytic Hydrogen Generation. Advanced materials (Deerfield Beach, Fla). 2015;27.
47. Bian J, Li J, Kalytchuk S, Wang Y, Li Q, Lau TC, et al. Efficient Emission Facilitated by Multiple Energy Level Transitions in Uniform Graphitic Carbon Nitride Films Deposited by Thermal Vapor Condensation. ChemPhysChem. 2015;16(5):954-9.
48. Xu J, Zhang L, Shi R, Zhu Y. Chemical exfoliation of graphitic carbon nitride for efficient heterogeneous photocatalysis. Journal of Materials Chemistry A. 2013;1(46):14766-72.
49. Gao J, Zhou Y, Li Z, Yan S, Wang N, Zou Z. High-yield synthesis of millimetre-long, semiconducting carbon nitride nanotubes with intense photoluminescence emission and reproducible photoconductivity. Nanoscale. 2012;4(12):3687-92.
50. Makuła P, Pacia M, Macyk W. How To Correctly Determine the Band Gap Energy of Modified Semiconductor Photocatalysts Based on UV–Vis Spectra. The Journal of Physical Chemistry Letters. 2018;9(23):6814-7.
51. Zhang Y, Pan Q, Chai G, Liang M, Dong G, Zhang Q, et al. Synthesis and luminescence mechanism of multicolor-emitting g-C3N4 nanopowders by low temperature thermal condensation of melamine. Scientific Reports. 2013;3(1):1943.
52. Zhang G, Zhang M, Ye X, Qiu X, Lin S, Wang X. Iodine modified carbon nitride semiconductors as visible light photocatalysts for hydrogen evolution. Advanced Materials. 2014;26(5):805-9.
53. Liu F, Kar S. Quantum Carrier Reinvestment-Induced Ultrahigh and Broadband Photocurrent Responses in Graphene–Silicon Junctions. ACS Nano. 2014;8(10):10270-9.
54. Zeng L, Tao L, Tang C, Zhou B, Long H, Chai Y, et al. High-responsivity UV-Vis Photodetector Based on Transferable WS2 Film Deposited by Magnetron Sputtering. Scientific Reports. 2016;6(1):20343.
55. Soci C, Zhang A, Xiang B, Dayeh SA, Aplin DPR, Park J, et al. ZnO Nanowire UV Photodetectors with High Internal Gain. Nano Letters. 2007;7(4):1003-9.
56. Kao MC, Chen H, Young S-L, Kung CY, Lin CC. The effects of the thickness of TiO2 films on the performance of dye-sensitized solar cells. Thin Solid Films. 2009;517:5096–9.